Journal of Computational Physics 229 (2010) 9397–9417

Contents lists available at ScienceDirect

Journal of Computational Physics

journal homepage: www.elsevier.com/locate/jcp

Faster and more accurate transport procedures for HZETRN

T.C. Slaba [a,*], S.R. Blattnig [a], F.F. Badavi [b]

[a] NASA Langley Research Center, 2 West Reid St., MS 188E, Hampton, VA 23681, USA
[b] Christopher Newport University, 1 University Pl., Newport News, VA 23607, USA

ARTICLE INFO

Article history:
Received 6 May 2010
Received in revised form 3 September 2010
Accepted 6 September 2010
Available online 15 September 2010

Keywords:
Space radiation
Particle transport
Radiation exposure
Radiation transport
HZETRN

ABSTRACT

The deterministic transport code HZETRN was developed for research scientists and design engineers studying the effects of space radiation on astronauts and instrumentation protected by various shielding materials and structures. In this work, several aspects of code verification are examined. First, a detailed derivation of the light particle ($A \leqslant 4$) and heavy ion ($A > 4$) numerical marching algorithms used in HZETRN is given. References are given for components of the derivation that already exist in the literature, and discussions are given for details that may have been absent in the past. The present paper provides a complete description of the numerical methods currently used in the code and is identified as a key component of the verification process. Next, a new numerical method for light particle transport is presented, and improvements to the heavy ion transport algorithm are discussed. A summary of round-off error is also given, and the impact of this error on previously predicted exposure quantities is shown. Finally, a coupled convergence study is conducted by refining the discretization parameters (step-size and energy grid-size). From this study, it is shown that past efforts in quantifying the numerical error in HZETRN were hindered by single precision calculations and computational resources. It is determined that almost all of the discretization error in HZETRN is caused by the use of discretization parameters that violate a numerical convergence criterion related to charged target fragments below 50 AMeV. Total discretization errors are given for the old and new algorithms to 100 g/cm^2 in aluminum and water, and the improved accuracy of the new numerical methods is demonstrated. Run time comparisons between the old and new algorithms are given for one, two, and three layer slabs of 100 g/cm^2 of aluminum, polyethylene, and water. The new algorithms are found to be almost 100 times faster for solar particle event simulations and almost 10 times faster for galactic cosmic ray simulations.

Published by Elsevier Inc.

1. Introduction

As human exploration moves beyond Earth's orbit into radiation environments where measured data are sparse and testing is difficult, models will be heavily relied upon to make decisions regarding vehicle design and mission planning. This reliance on model results requires a systematic effort of verification, validation, and uncertainty quantification. Verification is the process of determining that a computational model accurately represents the underlying mathematical model and its solution; validation is the process of determining if the underlying mathematical model accurately represents physical reality, and uncertainty quantification is the process of identifying all relevant sources of uncertainties and quantifying their impact on the inputs and outputs of the model [13]. This paper addresses verification of the deterministic radiation transport

* Corresponding author. Address: Mail Stop 188E, NASA Langley Research Center, 2 West Reid St. B1205, Rm. 281, Hampton, VA 23681-2199, USA. Tel.: +1 757 864 1420; fax: +1 757 864 8094.
E-mail addresses: Tony.C.Slaba@nasa.gov (T.C. Slaba), Steve.R.Blattnig@nasa.gov (S.R. Blattnig), Francis.F.Badavi@nasa.gov (F.F. Badavi).

0021-9991/$ - see front matter Published by Elsevier Inc.
doi:10.1016/j.jcp.2010.09.010

code HZETRN (High charge (Z) and Energy TRaNsport) [26,27,30,18] with a focus on documentation, improving efficiency and stability, and quantifying discretization error through convergence testing.

Documentation is a critical component of verification [15] and has been emphasized in the NASA standard for modeling and simulation tools [13]. While there have been many papers published that describe the transport model and physical parameters [21–23,26,29,30,3] as well as the marching algorithms and numerical methods [25,26,29,30,9,10,16] used in HZETRN, various gaps still exist in the documentation. This statement is not a criticism of past efforts in developing or documenting HZETRN; rather, it is a reflection of an increased focus on model verification [13]. In this paper, a detailed review and derivation is given for the existing light particle (n, p, ^{2}H, ^{2}H, ^{3}He, ^{4}He) and heavy ion ($A > 4$) marching algorithms used in HZETRN. References are given for components of the derivation that already exist in the literature, and discussions are given for details that may have been absent in the past. As a result of the review, a numerical convergence criterion is identified that, to the authors' knowledge, has yet to be documented or examined. It is shown later in the paper that the discretization parameters (spatial step-size and energy grid-size) commonly used in HZETRN violate this criterion and cause a systematic under-prediction of light charged target fragments below 50 AMeV.

This detailed derivation and review of the numerical methods also resulted in the development of a new light particle marching algorithm that is almost 100 times faster than its predecessor for solar particle event (SPE) simulations. Though computational efficiency (compared to Monte Carlo approaches) has long been a core feature of HZETRN, there were certain extreme applications for which the existing algorithms resulted in long run-times. For example, consider the interpolation or ray-by-ray methods used to compute mass averaged quantities in human phantoms exposed to space radiation. Interpolation methods are quite fast once the interpolation database has been generated, but in an extreme case, it takes the current code over seven hours to generate a detailed database on a single processor. Similarly, the ray-by-ray method can take over 20 h to compute the mass averaged particle fluence spectra at a single point in the body on a 192 core cluster. Approximately 1000 body points have been identified by Slaba et al. [19] as sufficient for computing whole body effective dose in human phantoms exposed to SPE and galactic cosmic rays (GCR)-indicating a significant computational cost. To help reduce these run-times and increase code efficiency, a new numerical method is presented for the light particle marching algorithm that reduces the required number of interpolations and removes the need for integral fluence to be calculated at each step. Run time comparisons between the old and new algorithms are given for one, two, and three layer slabs of 100 g/cm^2 of aluminum, polyethylene, and water. The new algorithms are found to be almost 100 times faster for solar particle event (SPE) simulations and almost 10 times faster for galactic cosmic ray (GCR) simulations.

Controlling round-off error is another important component of code verification. Though previous convergence studies [16,20] and benchmark comparisons [24,26,29,30,6,7] would indicate that round-off error has already been controlled, such comparisons were generally made at moderate shielding depths where round-off errors are assumed to be small. However, as HZETRN is increasingly used in atmospheric and surface applications with large material thicknesses (>50 g/cm^2) [12,28], round-off error could be a major concern and needs to be investigated. Selected light particle cross sections are calculated in single and double precision, and the impact of round-off error in the single precision calculations is shown to be large in certain cases. The interpolation routine [27] frequently used in the transport algorithms is also examined, and a new routine is developed that is faster, has improved extrapolation procedures, and has the capability of interpolating around certain discontinuities. The improved code stability attained by using double precision calculations and the improved interpolation routine is demonstrated.

Finally, in many computational models or algorithms, continuous variables are discretized to reduce a differential equation into an algebraic expression that is evaluated numerically. The algorithm is said to converge if the numerical solutions reach an asymptotic limit as the discretization parameters approach zero. In order to show convergence and quantify discretization error, the discretization parameters are refined several times and the differences between the various solutions are compared. Such studies are often referred to as convergence tests. As part of a larger verification and validation effort, configuration controlled convergence tests are created which can be re-run when significant changes are made to the codes. The ability to re-run such tests will help prevent the introduction of errors into the code as modifications are made in the future. In HZETRN, the spatial variable x and energy variable E are discretized. Two convergence tests have previously been published [16,20]; however, those tests were primarily focused on verifying code stability and were limited by computational resources. In the first analysis, Shinn et al. [16] conducted a coupled convergence test in both space and energy. However, only two step-sizes (h = 0.5 g/cm^2 and h = 1.0 g/cm^2) and two energy grids (N = 30 and N = 60, where N is the number of grid points) were considered; only nucleons were transported, and all calculations were in single precision. No attempt was made to quantify discretization error, and numerical convergence was not clearly demonstrated. It should be noted that these early studies and early versions of HZETRN were executed on computers with limited capability by modern standards. Single precision calculations were used instead of double precision to reduce memory requirements and allow storage of large nuclear databases. In the more recent analysis, it was determined that at least 100 energy grid points are needed to control energy discretization error [20], but spatial discretization error was not considered. Neither the codes nor the results were configuration managed in these previous studies. It will be shown here that even step-sizes of h = 0.01 g/cm^2 can result in moderate errors for low energy target fragments with small residual ranges. In this work, a convergence study is conducted in both step-size and energy grid-size. The spatial discretization parameter, h, is reduced by factors of 2 from its common value of 0.5 g/cm^2 down to 2^{-11} g/cm^2. Similarly, the number of energy grid points is increased by factors of $\sim$1.5 from 100 up to 753. Particle fluence, dose, and dose equivalent values are then computed at various depths in aluminum and water slabs exposed to SPE and GCR environments using the old and new transport algorithms and each of the discretization

parameters. The resulting data are used to show that the new algorithms reach an asymptotic solution as the discretization parameters are refined. The improved accuracy of the new methods is also demonstrated. Discretization errors are also given for the discretization parameters commonly used in HZETRN ($h = 0.5$ g/cm^2 with 100 energy grid points). These errors are expressed as percent differences from the converged numerical solutions obtained with the finest discretization parameters.

2. Transport equations

In this section, the physical approximations used to obtain numerical procedures in HZETRN are reviewed. The time independent linear Boltzmann transport equation with the continuous slowing down and straight ahead approximations is given as [26]

$$\left[\frac{\partial}{\partial x} - \frac{1}{A_j}\frac{\partial}{\partial E}S_j(E) + \sigma_j(E)\right]\phi_j(x,E) = \sum_k \int_E^\infty \sigma_{jk}(E,E')\phi_k(x,E')dE', \tag{1}$$

with the boundary condition $\phi_j(0,E) = f_j(E)$. In Eq. (1), $\phi_j(x,E)$ is the fluence of type j particles at depth x with kinetic energy E, A_j is the atomic mass number of a type j particle, $S_j(E)$ is the stopping power of a type j ion with kinetic energy E, $\sigma_j(E)$ is the total macroscopic cross section for a type j particle with kinetic energy E, and $\sigma_{jk}(E,E')$ is the macroscopic differential production cross section for interactions in which a type k particle with kinetic energy E' produce a type j particle with kinetic energy E. The summation limits in Eq. (1) will be discussed shortly. The boundary condition spectrum, $f_j(E)$, is considered to be a known function over a broad energy spectrum. Throughout the rest of this paper, E is always the kinetic energy expressed in AMeV or AGeV (except for nucleons, where the "A" notation is unnecessary). The units of fluence for GCR environments are particles/(cm^2 AMeV day), and for SPE environments, the units of fluence are integrated over the event to obtain units of particles/(cm^2 AMeV).

Consider the continuous slowing down operator

$$\left[\frac{1}{A_j}\frac{\partial}{\partial E}S_j(E)\right]\phi_j(x,E), \tag{2}$$

which represents the rate at which charged particles lose energy as they interact with the electron clouds in the target media. Although atomic interactions cause charged particles to lose energy in discrete increments as they pass through a material, there are a sufficient number of these interactions in a unit path length to justify a continuous approximation [26]. It is advantageous to approximate this term by considering the relation from Bethe stopping power theory [2]

$$\nu_k r_k \approx \nu_j r_j, \tag{3}$$

where the scaling parameter is $\nu_j = Z_j^2/A_j$, with Z_j being the atomic charge of a type j particle, and the range of a type j ion, r_j, is given by the range–energy relationship

$$r_j \equiv A_j \int_0^E \frac{dE'}{S_j(E')}. \tag{4}$$

From Eqs. (3) and (4), the proton stopping power, S, can be approximated as

$$\nu_j S(E) \approx \frac{1}{A_j} S_j(E). \tag{5}$$

Eq. (5) is less accurate at low energy (<10 AMeV) or low residual range and has been discussed previously by Wilson et al. [26].

Eq. (5) allows the transport equation to be written as

$$\left[\frac{\partial}{\partial x} - \nu_j\frac{\partial}{\partial E}S(E) + \sigma_j(E)\right]\phi_j(x,E) = \sum_k \int_E^\infty \sigma_{jk}(E,E')\phi_k(x,E')dE'. \tag{6}$$

The motivation, justification, and physical implications associated with approximating each ion stopping power with a scaled proton stopping power has been discussed in detail elsewhere [30]. Ultimately, the approximation allows significant numerical simplifications, as will be shown later.

There are two paths taken (for light particles and heavy ions) in developing numerical procedures for Eq. (6). For heavy ions, it is noted that projectile fragments have energy and direction very near that of the projectile, while target fragments are produced nearly isotropically with low energy and travel only a short distance before being absorbed [22,23,26,27,30]. The approximate decoupling of target and projectile fragments is discussed in detail by Wilson et al. [22,26,27] and suggests that target fragments can be neglected in the heavy ion transport procedure (their contribution to dose is approximately accounted for after the transport procedure). The equal velocity assumption for heavy ions can be expressed in the production cross section as [17]

$$\sigma_{jk}(E,E') = \sigma_{jk}(E')\delta(E-E'), \tag{7}$$

where $\sigma_{jk}(E)$ is the production cross section for interactions in which a type k particle with kinetic energy E produce a type j particle. The absence of target fragments in the heavy ion transport procedure allows one to take the summation in Eq. (6) over all projectiles with mass greater than that of the fragment. If all the transported particles are ordered according to mass, then Eq. (6) can be succinctly written as

$$\left[\frac{\partial}{\partial x} - v_j \frac{\partial}{\partial E} S(E) + \sigma_j(E)\right] \phi_j(x,E) = \sum_{k>j} \sigma_{jk}(E)\phi_k(x,E), \tag{8}$$

which is the transport equation found in Wilson et al. [23,26,27,30] and will be referred to as the heavy ion transport equation. The upper summation limit in Eq. (8) can vary, but it is common to use no fewer than 59 ions. See Cucinotta et al. [4] for a discussion of isotope selection.

Alternatively, for light particles ($n, p, {}^2\mathrm{H}, {}^2\mathrm{H}, {}^3\mathrm{He}, {}^4\mathrm{He}$) both projectile and target fragments are included in the transport procedure. The broad energy distribution in collision events also indicates that the equal velocity assumption in Eq. (7) cannot be used. In this case, no simplifications to Eq. (6) are used, and the summation is taken over all light particles. Hereafter, Eq. (6) will be referred to as the light particle transport equation which includes both neutrons and light ions. It should be noted that for SPE environments with a negligible heavy ion component, only the solution to the light particle transport equation is required. For GCR environments, there are both heavy ion and light ion components, and solutions to the light particle and heavy ion transport equations must be evaluated simultaneously. The coupling of these two equations will be discussed later.

3. Light particle marching equation

The following formulation of the light particle marching equation was taken from Wilson et al. [21,25,26,30], Shinn et al. [16], Lamkin et al. [9,10], Cucinotta [3]. A detailed derivation with references has been given by Slaba et al. [18]. Further references in this section will be given only for mathematical techniques and physical arguments.

To develop a numerical marching procedure for the light particle transport equation, the differential operator on the left hand side of Eq. (6) is inverted using the method of characteristics [5]. To perform the inversion, define the scaled fluence and scaled production cross section

$$\psi_j(x,r) \equiv \bar{v}_j S(E)\phi_j(x,E) \tag{9}$$

$$s_{jk}(r,r') \equiv S(E)\sigma_{jk}(E,E'), \tag{10}$$

where the proton range, r, is defined in terms of the proton stopping power, $S(E)$, by the range–energy relationship in Eq. (4), and the modified scaling parameter is given by

$$\bar{v}_j \equiv \begin{cases} 1, & j = n, \\ v_j, & j \neq n. \end{cases} \tag{11}$$

The quantity $\bar{v}_j$ is used in fluence scaling to avoid a trivial solution for the neutrons. Notice that we have used the scaled proton range in Eq. (9) to allow the function $\psi_j(x,r)$ to be defined over the common proton range, r, for each particle type j.

The light particle transport equation is given in terms of the scaled quantities as

$$\left[\frac{\partial}{\partial x} - v_j \frac{\partial}{\partial r} + \sigma_j(r)\right] \psi_j(x,r) = \sum_k \frac{\bar{v}_j}{\bar{v}_k} \int_r^\infty s_{jk}(r,r')\psi_k(x,r')dr', \tag{12}$$

where the term $\sigma_j(E)$ has been replaced with $\sigma_j(r)$, since for a given value of r, Eq. (4) can be inverted to determine E. Note that even though several values of E may map to the same value of $S(E)$, the function, $r(E)$, defined by the integral in Eq. (4), is one-to-one. Thus, the inverse mapping from E to r is well defined.

Eq. (12) is inverted using the method of characteristics to obtain a Volterra integral equation and written as an implicit marching procedure in terms of the step-size, h, as

$$\psi_j(x+h,r) = e^{-\beta_j(r,h)}\psi_j(x,r+v_j h) + \sum_k \frac{\bar{v}_j}{\bar{v}_k} \int_0^h \int_{r+v_j x'}^\infty e^{-\beta_j(r,x')} s_{jk}(r+v_j x', r')\psi_k(x+h-x', r')dr'dx', \tag{13}$$

with the integrating factor defined

$$\beta_j(r,x) \equiv \int_0^x \sigma_j(r+v_j t)dt. \tag{14}$$

The scaled fluence on the left hand side of Eq. (13) represents particles at position $x + h$ with range r. The scaled fluence on the right hand side represents particles at position x with a range (energy) downshift caused by atomic interactions within the step-size, and the multiplied exponential term represents attenuation due to nuclear absorption. The summation and integral terms represent production of light particles with nuclear attenuation and atomic slowing down over the step-size. The scaled fluence in the integrand of Eq. (13) is approximated as [26]

$$\psi_j(x+h,r) = e^{-\beta_j(r,h)}\psi_j(x,r+v_j h) + O(h). \tag{15}$$

The scaled fluence on the left hand side represents particles at position $x + h$ with range r. The scaled fluence on the right hand side represents particles at position x with range $r + v_j h$, with the difference in range values representing an energy down shift caused by atomic interactions within the step-size. The exponential term represents attenuation due to nuclear absorption. Eq. (15) without the $O(h)$ term is the exact solution to the homogeneous form of Eq. (12). The homogeneous equation neglects secondary particle production through nuclear interactions and accounts only for the slowing down of particles due to atomic interactions and the loss of particles due to nuclear absorption. If the step-size is taken to be sufficiently small such that

$$h \ll \frac{1}{\sigma_j(r)} \tag{16}$$

(i.e. much less than the nuclear mean free path), then the local truncation error will be negligible as the particles will not have travelled far enough to suffer a nuclear collision [26]. Eq. (16) is the first convergence criterion and has been well documented in the literature [21,25,26,30]. It is worth noting that nuclear mean free path lengths are on the order of many g/cm^2, while the step-sizes usually taken in HZETRN are less than 1 g/cm^2.

Eq. (15) is used to approximate the integrand in Eq. (13) [21,25,26,30]. This approximation produces the explicit marching procedure for light particles

$$\begin{aligned}\psi_j(x+h,r) &= e^{-\beta_j(r,h)}\psi_j(x,r+v_j h) \\ &\quad + \sum_k \frac{\bar{v}_j}{\bar{v}_k}\int_0^h \int_{r+v_j x'}^{\infty} e^{-\beta_j(r,x')-\beta_k(r',h-x')} s_{jk}(r+v_j x', r')\psi_k(x, r'+v_k(h-x'))dr'dx' + O(h^2),\end{aligned} \tag{17}$$

where the $O(h^2)$ terms are small. This is the light particle marching equation given by Wilson et al. [30] for which numerical procedures will be developed and studied later. Hereafter, the $O(h^2)$ will be assumed in the marching equations and not written.

4. Heavy ion marching equation

The following derivation of the heavy ion marching equation was taken from Wilson et al. [22,23,26,27,30] and Shinn et al. [17]. A detailed derivation with references has been given by Slaba et al. [18]. Further references will only be given for mathematical techniques. Any variables and symbols used in this section that were defined in the previous section hold their respective definitions.

The heavy ion trzansport equation was given previously in Eq. (8). The heavy ion fluences are scaled with $v_j S(E)$, and the term $\sigma_{jk}(E)$ is replaced with $\sigma_{jk}(r)$ since, for a given r, Eq. (4) can be inverted to find E. Following the procedure outlined in the previous section, Eq. (8) is written in terms of the scaled fluence and inverted using the method of characteristics to obtain a Volterra type integral equation. The integral equation is then written as an implicit marching procedure in terms of the step-size, h, as

$$\begin{aligned}\psi_j(x+h,r) &= e^{-\beta_j(r,h)}\psi_j(x,r+v_j h) \\ &\quad + \sum_{k>j} \frac{v_j}{v_k}\int_0^h e^{-\beta_j(r,x')}\sigma_{jk}(r+v_j x')\psi_k(x+h-x', r+v_j x')dx'.\end{aligned} \tag{18}$$

The scaled fluence on the left and right hand sides of Eq. (18) have the same physical meanings as in Eq. (13); however, the summation and integral terms represent production and transport of projectile fragments with nuclear attenuation and atomic slowing down over the step-size. As before, the $O(h)$ homogenous solution [30] is used to approximate the scaled fluence in the integrand to obtain the final marching procedure

$$\begin{aligned}\psi_j(x+h,r) &= e^{-\beta_j(r,h)}\psi_j(x,r+v_j h) \\ &\quad + \sum_{k>j} \frac{v_j}{v_k}\int_0^h e^{-\beta_j(r,x')-\beta_k(r+v_j x', h-x')}\sigma_{jk}(r+v_j x')\psi_k(x, r+v_j x'+v_k(h-x'))dx' + O(h^2).\end{aligned} \tag{19}$$

The integral over x' from 0 to h is approximated by expanding the production cross section and scaled fluence in a Taylor series neglecting all second order terms. The remaining integrals in the argument of the exponentials are similarly handled by expanding in a Taylor series neglecting all second order terms. This approximation allows the integral to be evaluated exactly, resulting in the final marching procedure given by

$$\begin{aligned}\psi_j(x+h,r) &= e^{-\beta_j(r,h)}\psi_j(x,r+v_j h) \\ &\quad + \sum_{k>j} \frac{v_j}{v_k}\sigma_{jk}(r+v_j h/2)\psi_k(x, r+(v_j+v_k)h/2)\frac{e^{-\sigma_j(r+v_j h/2)h} - e^{-\sigma_k(r+(v_j+v_k)h/2)h}}{\sigma_k(r+(v_j+v_k)h/2) - \sigma_j(r+v_j h/2)} + O(h^2),\end{aligned} \tag{20}$$

where the $O(h^2)$ terms are small. This is the heavy ion marching equation given by Wilson et al. [30] for which numerical procedures will be studied later. Hereafter, the $O(h^2)$ will be assumed in the marching equations and not written.

5. Existing light particle marching equation numerical methods

In this section, the numerical methods developed to evaluate Eq. (17) are reviewed, and the error analysis found in the literature for those methods is summarized. The following notation and terminology will be used extensively throughout the remainder of the paper. An energy grid (E-grid) refers to a discrete set of energy values distributed in some manner between a minimum energy value, $E_{\min}$, and a maximum energy value, $E_{\max}$. The ith component of the E-grid is denoted as E_i. A range grid (r-grid) refers to a discrete set of proton range values distributed in some manner between a minimum range value, $r_{\min}$, and a maximum range value, $r_{\max}$. The ith component of the r-grid is denoted as r_i. The number of grid points in a grid, or grid-size, is denoted by N. It will be assumed that all grid indexing is from $i = 1$ to $i = N$. Equal-log spacing is also used extensively; the ith component of an equal-log spaced E-grid is evaluated as

$$E_i = 10^{\log(E_{\min})+\Delta_E(i-1)}, \tag{21}$$

where the energy spacing parameter is defined as

$$\Delta_E \equiv \frac{\log(E_{\max}) - \log(E_{\min})}{N-1}, \tag{22}$$

and the logarithms are base 10. Note that an energy grid can be converted to a range grid, and vice versa, using Eq. (4).

In the light particle marching Eq. (17), the quantity $\psi_j(x, r + v_j h)$ will have to be evaluated for range values not on the prescribed r-grid. Wilson et al. [26] and Lamkin et al. [9] have shown that a log–log cubic Lagrange interpolating polynomial provides sufficient accuracy with a minimal number of grid points. The terminology "log–log" refers to taking the logarithm of both the dependent and independent variables prior to interpolating. The interpolated value is then exponentiated to adjust for the initial logarithm. It has been shown that higher order Lagrange polynomials offer little more in accuracy, and higher order splines can introduce uncontrollable oscillatory behavior that is problematic in marching procedures [9].

To evaluate the source integrals, the integral over x' from 0 to h is simplified by using a modified single point midpoint rule for integrable functions $a(x)$, $b(x)$, and $c(x)$ of the form

$$\int_0^h a(x)b(x)c(x)dx \approx a(h/2)\left[\int_0^h b(x)dx\right]c(h/2). \tag{23}$$

This approximation will be accurate if the functions $a(x)$ and $c(x)$ are nearly constant over the interval $[0, h]$. When applied to Eq. (17), this approximation yields [26,30]

$$\psi_j(x+h,r) = e^{-\beta_j(r,h)}\psi_j(x, r+v_j h) + \sum_k \frac{\bar{v}_j}{\bar{v}_k}\int_{r+v_j h/2}^{\infty} e^{-\beta_j(r,h/2)-\beta_k(r',h/2)}\left[\int_0^h s_{jk}(r+v_j x', r')dx'\right]\psi_k(x, r'+v_k h/2)dr'. \tag{24}$$

The modified midpoint rule has decoupled the source integrals in Eq. (17); however, the approximation will only be accurate if the step-size is sufficiently small to satisfy

$$h \ll r/v_j \approx r_j. \tag{25}$$

Eq. (25) is the second convergence criterion. Recall that the first criterion was identified previously in Eq. (16) and required the step-size to be smaller than the nuclear mean free path length. The second criterion in Eq. (25) is a numerical constraint that only exists because of the approach taken to decouple the source integrals in the light particle marching equation. To the authors' knowledge, this second criterion has never been explicitly stated or addressed in the literature. To put the second criterion in context, note that the range of a 100 MeV proton produced in aluminum is $\sim$10 g/cm^2, so a step-size of 0.5 g/cm^2 will be sufficient in this approximation. However, a 10 MeV proton produced in aluminum will travel $\sim$0.17 g/cm^2 before coming to rest, and a 1 MeV proton produced in aluminum will travel $\sim$0.004 g/cm^2 before coming to rest. This indicates that step-sizes of 0.5 g/cm^2 and 1.0 g/cm^2 studied previously [16] do not accurately transport low energy target fragments. It will be shown later that even step-sizes near 0.01 g/cm^2 will systematically under-predict the source integral by neglecting the particle production from projectiles with low ranges near that of fragments. This approximation will be tested in detail when the coupled energy grid and step-size convergence study is conducted.

The light particle transport equation is further simplified for charged particle fragments

$$\int_0^h s_{jk}(r+v_j x', r')dx' = \frac{1}{v_j}\left[\int_0^{\varepsilon(r+v_j h)}\sigma_{jk}(E,E')dE - \int_0^{\varepsilon(r)}\sigma_{jk}(E,E')dE\right] \equiv F_{jk}^{\Delta}(r, r'; h). \tag{26}$$

The term $\varepsilon(r)$ is the energy associated with the proton range r. For neutron fragments, denoted by $j = n$,

$$\int_0^h s_{nk}(r+v_n x', r')dx' = h s_{nk}(r, r') \equiv F_{nk}^{\Delta}(r, r'; h). \tag{27}$$

The remaining exponential attenuation terms in Eq. (24) are simplified by using a first order series expansion [16,9]. These approximations are exact for neutrons and have been shown [16,9] to produce negligible errors for charged particles with step-sizes up to $h = 0.5$ g/cm^2. The light particle transport equation is now reduced to

$$\psi_j(x+h,r) = e^{-\sigma_j(r)h}\psi_j(x,r+v_jh) + \sum_k \frac{\bar{v}_j}{\bar{v}_k}\int_{r+v_jh/2}^{\infty} e^{-\sigma_j(r)h/2-\sigma_k(r')h/2}F_{jk}^{\Delta}(r,r';h)\psi_k(x,r'+v_kh/2)dr'. \tag{28}$$

The final integral is simplified by considering a composite quasi-midpoint rule defined over several sub-intervals within a given region

$$\int_a^b f(x)g(x)dx \approx \sum_{i=1}^{N-1} f(\bar{x}_i)\int_{x_i}^{x_{i+1}} g(x)dx, \tag{29}$$

where $x_1 = a$, $x_N = b$, and $\bar{x}_i = (x_{i+1}+x_i)/2$. This approximation is similar to the multi-group method commonly used in nuclear reactor transport theory and requires the sub-intervals $[x_i,x_{i+1}]$ to be sufficiently small such that $f(x)$ is nearly constant over the sub-interval [11]. The composite quasi-midpoint rule in Eq. (29) can be applied to the integral in Eq. (28) to obtain

$$\psi_j(x+h,r_i) = e^{-\sigma_j(r_i)h}\psi_j(x,r_i+v_jh) + \sum_k \frac{\bar{v}_j}{\bar{v}_k}\sum_{m=i}^{N-1} e^{-\sigma_j(r_i)h/2-\sigma_k(r_m)h/2}F_{jk}^{\Delta}(r_i,\bar{r}_m+v_jh/2;h)\left[\Psi_j(x,r_m+(v_j+v_k)h/2)-\Psi_j(x,r_{m+1}+(v_j+v_k)h/2)\right], \tag{30}$$

where the integral fluence is defined as

$$\Psi_j(x,r) \equiv \int_r^{\infty}\psi_j(x,r'')dr'' = \bar{v}_j\int_E^{\infty}\phi_j(x,E'')dE'', \tag{31}$$

and $\bar{r}_m \equiv (r_{m+1}+r_m)/2$. Slaba et al. [20] have recently shown this approximation to be poor for neutron elastic interactions in which the energy loss between the pre-collision and post-collision neutron is very small. They have modified the neutron elastic component, $F_{nn}^{\Delta,el}$, so that it is now evaluated as

$$F_{nn}^{\Delta,el}(r_i,\bar{r}_m;h) = hS(E)\langle\sigma_{nn}^{el}(r_i,\bar{r}_m)\rangle, \tag{32}$$

with the average value of the neutron elastic production cross section is defined over the interval $[r_m,r_{m+1}]$

$$\langle\sigma_{nn}^{el}(r_i,\bar{r}_m)\rangle \equiv \frac{1}{\varepsilon(r_{m+1})-\varepsilon(r_m)}\int_{\varepsilon(r_m)}^{\varepsilon(r_{m+1})}\sigma_{nn}^{el}(\varepsilon(r_i),E')dE'. \tag{33}$$

In Eq. (33), $\varepsilon(r)$ denotes the energy associated with the range value r. Eqs. (30)–(33) define the light particle marching procedure used in HZETRN and tested in this report. Two things should be noted about the original light particle marching equation. First, evaluation of Eq. (30) requires the integral fluence to be computed and interpolated for each particle at each step. Second, historically, in this algorithm, *all* of the computations were carried out in single precision due to computational constraints, as discussed previously. More will be said about both of these points later.

6. New light particle marching equation numerical methods

In this section, new numerical methods are presented to evaluate the light particle marching equation. The approximations used in the previous section to get from Eqs. (17)–(28) are all used in this section; therefore, we begin with Eq. (28) and change integration variables so that the light particle transport equation becomes

$$\psi_j(x+h,r) = e^{-\sigma_j(r)h}\psi_j(x,r+v_jh) + \sum_k \int_r^{\infty} e^{-\sigma_j(r)h/2-\sigma_k(r'-v_kh/2)h/2}\overline{F}_{jk}^{\Delta}(r,r'-v_kh/2;h)\psi_k(x,r')dr', \tag{34}$$

where we include the scaling parameters in the definition of the integrated light particle cross sections

$$\overline{F}_{jk}^{\Delta}(r,r';h) \equiv \frac{\bar{v}_j}{\bar{v}_k}F_{jk}^{\Delta}(r,r';h). \tag{35}$$

In the new method, the scaled fluence in the integrand, $\psi_k(x,r')$, is approximated by a linear combination of log-linear basis splines as

$$\psi_k(x,r') \approx \sum_{m=1}^{N} B_m^{(l)}(r')\psi_k(x,r_m), \tag{36}$$

with the log-linear spline

$$B_m^{(l)}(r) = \begin{cases} \ln(r/r_{m-1})/\ln(r_m/r_{m-1}), & r \in [r_{m-1}, r_m], \\ \ln(r_{m+1}/r)/\ln(r_{m+1}/r_m), & r \in [r_m, r_{m+1}], \\ 0, & \text{otherwise}. \end{cases} \tag{37}$$

Upon substitution of Eq. (36) into Eq. (34) one obtains

$$\psi_j(x+h,r) = e^{-\sigma_j(r)h}\psi_j(x, r+v_j h) + \sum_k \sum_{m=1}^{N} \psi_k(x, r_m) \int_{r+(v_j+v_k)h/2}^{\infty} e^{-\sigma_j(r)h/2 - \sigma_k(r'-v_k h/2)h/2} \overline{F}_{jk}^{A}(r, r' - v_k h/2; h) B_m^{(l)}(r') dr'. \tag{38}$$

In Eq. (38), the integrand and the integral no longer depend on the scaled fluence or the depth in the material. The integral can be treated as a constant matrix of production coefficients depending only on the step-size and the r-grid. If we evaluate Eq. (38) at the ith r-grid value, then the production coefficients can be defined as

$$a_{im}(h) \equiv \int_{r_i+(v_j+v_k)h/2}^{\infty} e^{-\sigma_j(r_i)h/2 - \sigma_k(r'-v_k h/2)h/2} \overline{F}_{jk}^{A}(r_i, r' - v_k h/2; h) B_m^{(l)}(r') dr', \tag{39}$$

so that the transport equation is now greatly simplified

$$\psi_j(x+h, r_i) = e^{-\sigma_j(r_i)h}\psi_j(x, r_i + v_j h) + \sum_k \sum_{m=1}^{N} a_{im}(h)\psi_k(x, r_m). \tag{40}$$

This approach casts the production integral as a linear combination of terms computed on the original r-grid requiring no further interpolation or integration.

The production coefficients, a_{im}, are further simplified by noting that the basis spline, $B_m^{(l)}(r')$, is non-zero only in the region $[r_{m-1}, r_{m+1}]$. Therefore,

$$a_{im}(h) = \int_{r_a}^{r_b} e^{-\sigma_j(r_i)h/2 - \sigma_k(r'-v_k h/2)h/2} \overline{F}_{jk}^{A}(r_i, r' - v_k h/2; h) B_m^{(l)}(r') dr', \tag{41}$$

where the limits of integration are defined

$$r_a \equiv \max\{r_i + (v_j + v_k)h/2, r_{m-1}\}, \tag{42}$$

$$r_b \equiv \min\{r_N, r_{m+1}\}, \tag{43}$$

and min and max refer to the minimum and maximum values, respectively. For neutron elastic interactions, the upper limit has been adjusted to

$$r_b \equiv \min\{r_N, r_{m+1}, r_\alpha\}, \tag{44}$$

where r_α is the proton range associated with the energy $E_\alpha = \varepsilon(r_i)/\alpha_T$, $\varepsilon(r_i)$ is the energy associated with the proton range r_i, and α_T is the target dependent parameter given by

$$\alpha_T = \left(\frac{A_T - 1}{A_T + 1}\right)^2, \tag{45}$$

and A_T is the mass of the target nucleus. To understand from where the term r_α was taken, note that Wilson et al. [26] have parameterized the neutron elastic production cross section to be non-zero in the energy region

$$\alpha_T E' < E < E', \tag{46}$$

where E' is the energy of the pre-collision neutron, and E is the energy of the post-collision neutron. For heavy targets, in which $\alpha_T \to 1$, the non-zero region of the neutron elastic production cross section can become smaller than the spacing of the E-grid (or r-grid). Including the upper bound of the elastic cross section in the selection of the upper limit of integration will properly account for such occurrences.

Similarly, for quasi-elastic interactions involving ^{4}He projectiles, the lower limit of integration has been adjusted to

$$r_a = \max\left\{r_i + (v_j + v_k)h/2, r_{m-1}, r_i^{(B)} + h/2\right\}, \tag{47}$$

where $r_i^{(B)}$ is the proton range associated with the energy $\varepsilon(r_i) + E_B$, and E_B is the binding energy of the struck nucleus. The term $r_i^{(B)} + h/2$ was obtained by noting that in ^{4}He quasi-elastic interactions, secondary ^{4}He ions have energy E bounded above by the difference between the projectile energy, E′, and the binding energy of the struck nucleus, E_B. In Eq. (41), the cumulative production cross section, $\overline{F}_{jk}^{A}$, is evaluated at $r' - v_k h/2$, and since $v_k = 1$ for ^{4}He, the minimum projectile energy must be $\varepsilon(r_i^{(B)} + h/2)$.

The production coefficients are evaluated using a 10-point Gauss Legendre integration scheme to obtain a high level of accuracy with a minimal number of quadrature points. Even though the numerical integrations are carried out over small sub-intervals of the r-grid, the production coefficients are still computationally expensive to calculate for a single h value; therefore, they are approximated by using the log-linear interpolation

$$a_{im}(h) \approx \exp\left\{a_{im}^{(l)}(h_{p+1}) + \left[a_{im}^{(l)}(h_{p+1}) - a_{im}^{(l)}(h_p)\right](h^{(l)} - h_p^{(l)})/(h_{p+1}^{(l)} - h_p^{(l)})\right\} \equiv a_{im}^{*}, \tag{48}$$

where $a_{im}^{(l)} \equiv \log(a_{im})$ and $h^{(l)} \equiv \log(h)$. This requires the coefficients $a_{im}(h)$ to be pre-computed for several values of h from 0.0 g/cm^2 to 0.5 g/cm^2. The h-grid has been taken to be

$$h_p = \{0.0, 0.001, 0.005, 0.01, 0.05, 0.1, 0.25, 0.5\}. \tag{49}$$

The values of h were chosen to adequately cover the necessary range of step-sizes, while minimizing the number of points.

The final marching equation for light particles is now written as

$$\psi_j(x + h, r_i) = e^{-\sigma_j(r_i)h}\psi_j(x, r_i + v_j h) + \sum_k \sum_{m=1}^{N} a_{im}^{*}\psi_k(x, r_m). \tag{50}$$

The new marching Eq. (50) is much simpler than the original Eq. (30). Specifically, there is no longer a need to compute or interpolate on integral fluence. The entire source calculation has been reduced to a simple matrix–vector multiplication. The most computationally expensive portion of the new algorithm is the interpolation at $r_i + v_j h$. The interpolation routine [27] used in previous versions of HZETRN was reviewed, and several modifications were made to improve efficiency and robustness. The updated routine still performs log–log cubic interpolation with Lagrange polynomials but is more efficient and has improved logic for interpolation around certain discontinuities and extrapolations past $r_{\max}$. A comparison of the routines will be given later. It should also be noted that in the new algorithm, all of the computations are carried out in double precision; the need for double precision will be shown later. The updated algorithm is much simpler and faster than its predecessor. An estimate of the improvements can be obtained by counting the number of interpolations in a single iteration of the light particle transport equation. Assuming there are six particles to transport and N grid points in the r-grid, the number of interpolations in the new algorithm scales linearly with N, while the old algorithm scales quadratically with N.

7. Heavy ion marching equation numerical methods and coupling for GCR

The heavy ion marching equation was given previously in Eq. (20). The only numerical technique required to evaluate this equation is interpolation. The interpolation routine used in the heavy ion marching algorithm [27] is the same routine used in the light particle marching algorithm. Thus, to improve efficiency and robustness, this routine has been replaced with the updated version mentioned in the previous section. A comparison of the routines will be given shortly.

The GCR environment is composed of energetic protons, alpha particles, and heavier ions with $Z > 2$. In order to simultaneously transport all of these particles using the methods outlined above, the light particle and heavy ion marching algorithms must be coupled. This coupling has never been explicitly documented, but has existed in HZETRN for some time. The complete marching algorithm for GCR environments can be succinctly written as

$$\begin{aligned}\psi_j(x + h, r_i) = {} & e^{-\sigma_j(r_i)h}\psi_j(x, r_i + v_j h) + H(J - j)\sum_k \sum_{m=1}^{N} a_{im}^{*}\psi_k(x, r_m) \\ & + \sum_{k>J_*} \frac{v_j}{v_k}\sigma_{jk}(r + v_j h/2)\psi_k(x, r + (v_j + v_k)h/2)\frac{e^{-\sigma_j(r+v_j h/2)h} - e^{-\sigma_k(r+(v_j+v_k)h/2)h}}{\sigma_k(r + (v_j + v_k)h/2) - \sigma_j(r + v_j h/2)}.\end{aligned} \tag{51}$$

The index J refers to the heaviest light ion (^{4}He), the function $H(J - j)$ is the Heaviside function, and the lower limit of the single summation term is $J^{*} = \max\{j, J\}$. The double summation term is the source calculation for light projectiles and light fragments using the new method described in the previous section. Eq. (51) can be written in terms of the old light particle marching algorithms by replacing the double summation term in Eq. (51) with the double summation in Eq. (30).

The physical interpretation of Eq. (51) is straightforward. The double summation term is the source for light particles produced from light projectiles and is only evaluated if the particle subscript j refers to a light particle. The single summation term is the source for light and heavy projectile fragments produced from heavy ion projectiles. This is the coupling mechanism between the light particle and heavy ion transport equations.

8. Round-off error and interpolation

In this section, the impact of single precision round-off error and interpolation on exposure quantities and overall code stability is examined. First, the errors caused by single precision calculations in the light particle cross sections are analyzed. These errors are significant enough to cause instabilities in the transport algorithms that are problematic for material thicknesses >50 g/cm^2. Finally, the new interpolation routine mentioned in previous sections is compared to the original routine [27], and the improved efficiency and robustness of the updated algorithm is shown. Though this section points out the disadvantages of using single precision in the evaluation of the light particle production cross sections, it should be mentioned that single precision calculations were necessary in the early development of HZETRN in order to satisfy memory constraints that were common to computers of that time.

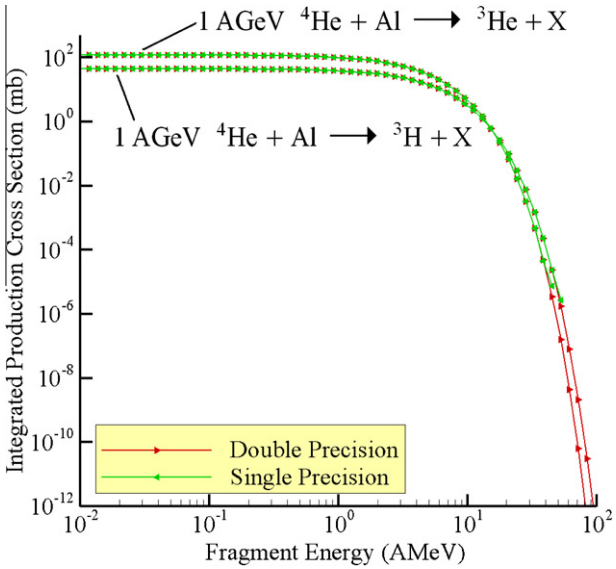

Fig. 1. Integrated production cross section for a 1 AGeV ^{4}He ion producing ^{3}He and ^{3}H in aluminum.

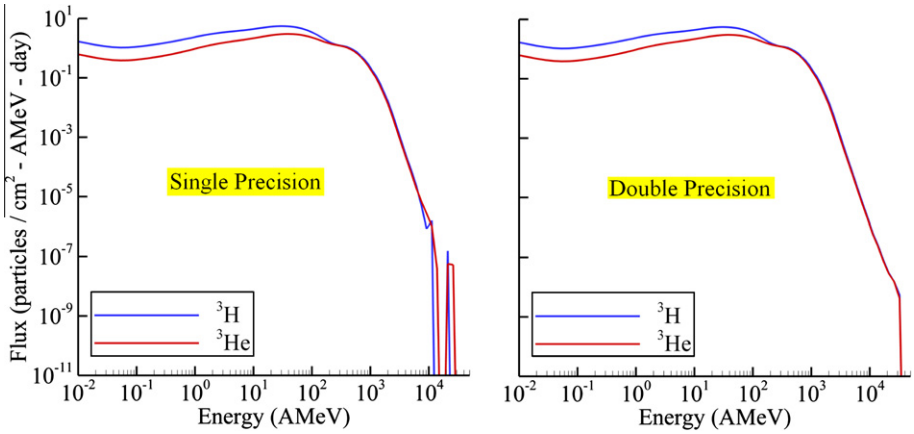

Fig. 2. Secondary ^{3}H and ^{3}He fluences computed using single and double precision cross sections at 100 g/cm^2 in aluminum exposed to the ^{4}He component of the 1977 solar minimum GCR spectrum.

Subtractive cancellation can occur in computational algorithms when the difference is computed between two numbers that are nearly equal in a given precision. This problem occurs for some of the light particle cross section calculations. The integrated light particle production cross sections, defined in Eq. (26), are computed as a difference of two cumulative production spectra. For large fragment energies, when $\varepsilon(r + v_j h) \approx \varepsilon(r)$, the two integrals in Eq. (26) become nearly equal. Thus, in single precision, the difference will lose numerical precision and may be evaluated as zero. An example of this is shown in Fig. 1, where the integrated light particle production cross section, $F^A_{jk}(r, r'; h)$, for 1 AGeV ^{4}He ions producing ^{3}H and ^{3}He in aluminum [3] are evaluated in single and double precision. For fragment energies larger than ~53 AMeV, the single precision results are zero and are therefore not visible on the plot. Similar results were also found for other reactions and projectile energies. The impact of this round-off error on particle fluence spectra can be seen in Fig. 2, where the secondary ^{3}H and ^{3}He fluences at 100 g/cm^2 in aluminum exposed to the ^{4}He component of the 1977 solar minimum GCR spectrum [14] are shown. The instabilities in the single precision results above 10 AGeV are clear. As these results are propagated to larger depths, the instabilities grow in magnitude, reach lower energies, and eventually cause algorithm failure.

Lastly, the interpolation routine used in previous versions of HZETRN is compared to a new interpolation routine that is faster and more robust. Both routines used cubic Lagrange interpolating polynomials. The interpolation routine previously used in the transport algorithms [27] performed log–log cubic interpolation and extrapolation. The search procedure used to find the abscissa points closest to the interpolation point was linear and searched in one direction from the origin (started from the first data point and searched forward one point at a time). All logarithms and exponentials were computed within

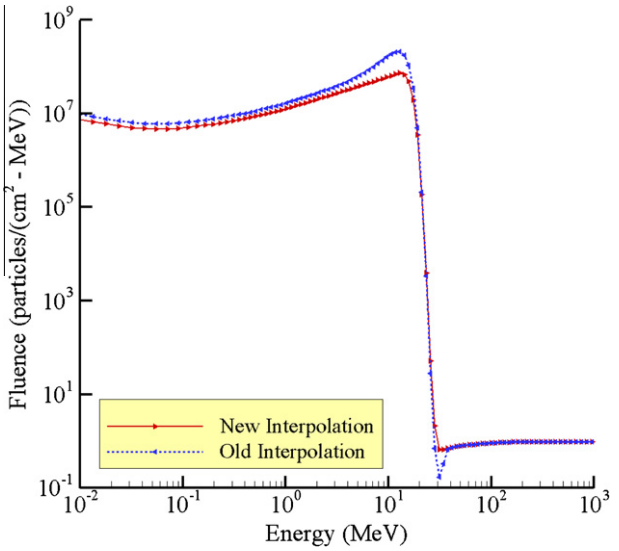

Fig. 3. Comparison of old and new interpolation routines in 2 g/cm^2 of aluminum exposed to a modified form of the August 1972 King SPE.

the algorithm. No logic was included to ensure that extrapolated results matched the trends of the data within the domain (i.e. increasing or decreasing). Also, no logic was included to check for non-smooth data.

In the updated algorithm, the search procedure used to find the abscissa points is linear and searches in either direction from the previously used interpolation point. Thus, when the routine is called repeatedly with an ordered or sequential set of interpolation points, the search algorithm uses previous results to find the nearest abscissa points. The new algorithm also avoids the use of logarithms and exponentials. Instead, the natural log of the data points is computed once prior to interpolation and used repeatedly. The extrapolation procedure has been switched to log–log linear. This will ensure that extrapolated results always match the trend of the data near the end of the domain. Logic has also been included to check for non-smooth data. In the event that the interpolated result does not lay between its nearest two data points, the interpolated value is re-computed using linear interpolation. Slaba et al. [18] have shown that the new routine is almost 3.5 times faster than its predecessor.

To show the improved robustness of the updated algorithm, a modified form of the August 1972 King SPE [8] is propagated through 2 g/cm^2 of aluminum using a step-size of $h = 0.5$ g/cm^2. The King spectrum was originally defined as $f_p(E) = N exp(-(E-30)/26.5)$, where the subscript p refers to protons and the constant $N = 2.98 \times 10^8$. The modified spectrum has been adjusted so that the proton fluence above 50 MeV is 1.0 particles/(cm^2 MeV). The results are shown in Fig. 3. Note that the original discontinuity imposed at 50 MeV (not shown) has been shifted to approximately 30 MeV because of atomic interactions in the target. The benefit of the added logic for non-smooth data is clear. The old algorithm over-predicts results below 30 MeV, especially near the discontinuity; it also sharply under-predicts the results just past the discontinuity. This oscillatory behavior is characteristic of cubic polynomials and can be problematic when such errors are propagated to larger depths. Conversely, the new algorithm properly interpolates through a discontinuity and introduces no oscillatory behavior.

9. Convergence study for light particle transport in SPE environments

In this section, the total discretization error associated with the old and new light particle transport algorithms in HZETRN is examined by conducting a detailed convergence analysis in both step-size (h) and energy grid-size (N). For all comparisons, the round-off errors and interpolation routines mentioned in the previous section have been fixed in the original algorithms. This will allow a direct comparison between the original and updated transport methods. The convergence analysis is completed by transporting the August 1972 King SPE spectrum through 100 g/cm^2 of aluminum and water. Six different energy grids were used with minimum and maximum energy values of $E_{min} = 0.01$ AMeV and $E_{max} = 2500$ AMeV. The grids were equally log spaced in energy and contained 100, 149, 223, 335, 502, and 753 points; these grids will be referred to as E-100, E-149, E-223, E-335, E-502, and E-753. Each grid represents a refinement of 1.5 in the grid spacing parameter defined in Eq. (22).

Along with these different energy grids, the following step-sizes (in g/cm^2) were used to propagate the boundary condition into the slabs: $h = 2^{-1}, 2^{-2}, 2^{-3}, \ldots, 2^{-11}$. Each step-size is a refinement of two in h. These eleven step-sizes, six energy grids, two materials, and two transport algorithms, were used to obtain fluence, dose, and dose equivalent values at various depths in the target media. These data are used to show that both algorithms converge as a function of step-size and energy grid-size for SPE boundary conditions. Total discretization error estimates are given for the discretization parameters

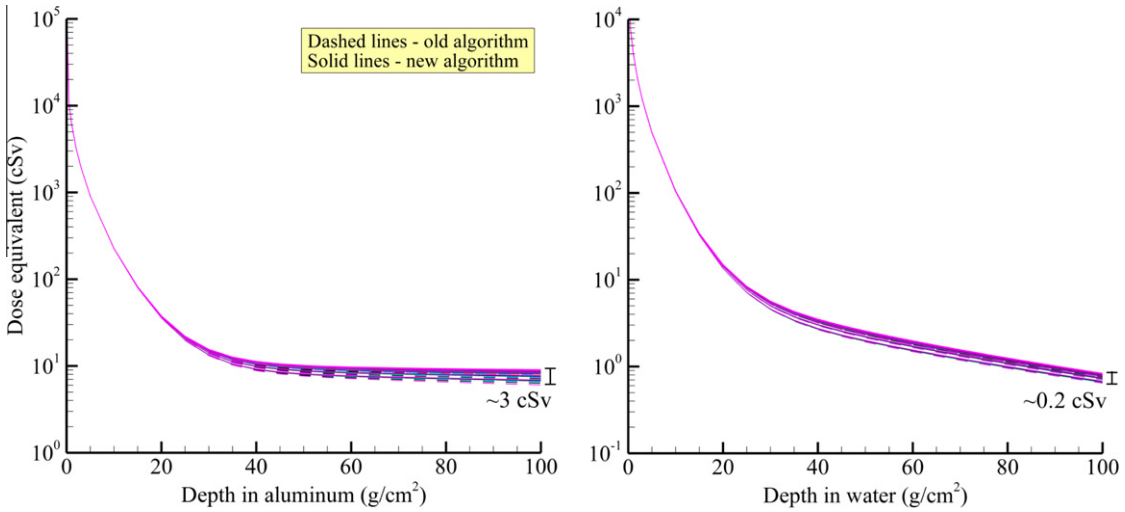

Fig. 4. Dose equivalent versus depth in aluminum (left pane) and water (right pane) exposed to the August 1972 King SPE computed with both transport algorithms and all discretization parameters.

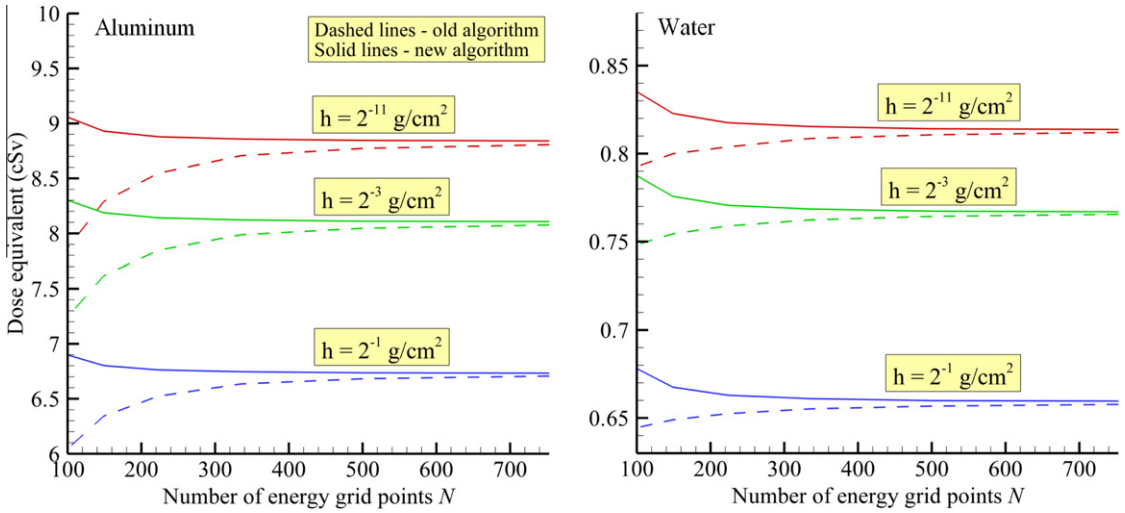

Fig. 5. Dose equivalent versus energy grid-size at 100 g/cm^2 in aluminum (left pane) and water (right pane) exposed to the August 1972 King SPE. Both transport algorithms were used with three different step-sizes.

(h = 0.5 g/cm^2 with 100 energy grid points) commonly used in HZETRN. The errors are expressed as percent difference from a converged numerical solution. It is also determined that the new algorithm is more accurate than its predecessor.

In Fig. 4, dose equivalent as a function of depth in aluminum and water is given for both of the algorithms and all of the discretization parameters. The plot legends have been removed because there are 132 different curves (6 energy grids, 11 step-sizes, 2 algorithms), many of which are overlapping. The spread in the data at 100 g/cm^2 in aluminum is ~3 cSv (~39%), and the spread in the data at 100 g/cm^2 in water is ~0.2 cSv (~26%). In these plots, both methods with the various discretization parameters produce similar results and the errors appear to be slowly increasing as a function of depth in the material. Slightly larger errors are also found in aluminum. These errors will be discussed in detail later.

In Fig. 5, the dose equivalent at 100 g/cm^2 in aluminum and water is plotted as a function of the energy grid-size, N, for three step-sizes. The three step-sizes were chosen to reduce data overlap and improve plot clarity. In Fig. 6, the dose equivalent at 100 g/cm^2 in aluminum and water is plotted as a function of the step-size, h, for all of the energy grids. Figs. 5 and 6 show that both algorithms reach an asymptotic solution for step-sizes less than 0.01 g/cm^2 and energy grids with greater than 300 points. The use of step-sizes larger than 0.01 g/cm^2 results in a systematic under-prediction of dose equivalent regardless of the method or energy grid used. The figures also show that if larger energy grids and smaller step-sizes were considered, the methods would generate almost identical solutions. The percent difference between the dose equivalent

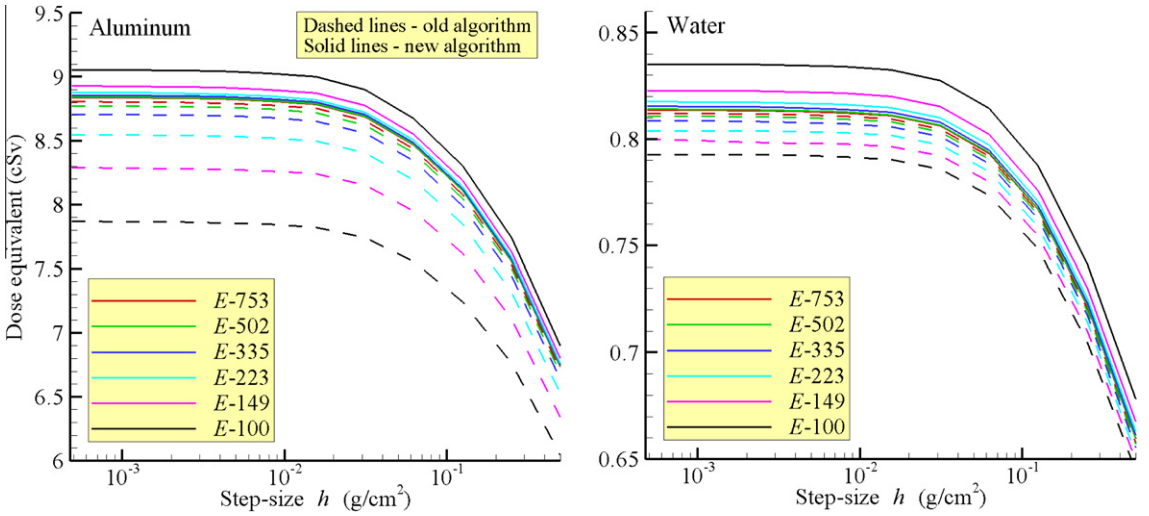

Fig. 6. Dose equivalent versus step-size at 100 g/cm^2 in aluminum (left pane) and water (right pane) exposed to the August 1972 King SPE. Both transport algorithms were used with six different energy grids.

values generated by the old and new algorithms with the finest discretization parameters ($h = 2^{-11}$, $N = 753$) is 0.4% at 100 g/cm^2 in aluminum and 0.2% at 100 g/cm^2 in water. Thus, it is concluded that both methods converge to the same value as a function of step-size and energy grid-size for this SPE in aluminum and water.

Fig. 6 indicates that there is little difference in spatial discretization error between the old and new algorithms. This is expected since the only difference between the algorithms is in the calculation of the source integral over energy. The new method appears to have a smaller energy discretization error in aluminum. This can be quantified by computing the percent difference between the *E*-100 and *E*-753 dose equivalent results from both algorithms with a step-size of $h = 2^{-11}$ g/cm^2 at 100 g/cm^2. The percent difference between the *E*-100 and *E*-753 results for the old algorithm is 10.7% in aluminum and 2.4% in water, while the percent difference between the *E*-100 and *E*-753 results for the new algorithm is 2.5% in aluminum and 2.6% in water. The improvement in aluminum was achieved primarily because the new algorithm more accurately handles the sharply peaked production cross sections in aluminum, especially the neutron elastic cross sections that are important at large depths. The negligible accuracy loss in water shows that the methods are comparable when the production cross sections are relatively smooth, as is the case when hydrogen is present.

While one would like to use the fully converged results in all future applications, the fine discretization parameters result in an inefficient algorithm that may be impractical. Thus, a smaller grid and larger step-size is chosen, and the results generated with these coarse discretization parameters are compared to the converged results to quantify the discretization error. As stated previously, HZETRN is commonly run with 100 energy grid points and a step-size of 0.5 g/cm^2. Therefore, $h = 0.5$ g/cm^2 and $N = 100$ are chosen as the coarse discretization parameters. The converged solution is defined as the results obtained with the new method using 753 energy grid points and a step-size of 2^{-11} g/cm^2. This choice is justified in Figs. 5 and 6 where it appears that both methods are asymptotically approaching a common solution. It is also important to note that the difference between the methods with the fine discretization parameters is very small. The discretization error is expressed as the percent difference between the results obtained with the coarse parameters and the converged solution. This expression of discretization error is relevant for space radiation applications where physics modeling errors, numerical errors, and uncertainties are often expressed in terms of percents. The results are given in Fig. 7. The new algorithm has a lower discretization error than the old algorithm out to 100 g/cm^2. This figure also shows that characteristically different errors are generated in aluminum and water targets.

Notice that in Fig. 7, there is a slight bend in the curves near 40 g/cm^2. This bend is the approximate depth at which the contribution to dose equivalent by the primary protons is overtaken by the contribution from secondary neutrons and charged target fragments, as shown in Fig. 8. In aluminum, the error curve continues to increase past the bend, while in water, the error curve decreases past the bend. This is due to the number and energy of secondary neutrons and charged target fragments produced in each material. In aluminum, there are a moderate number of neutrons produced as a result of nuclear collisions between the primary protons and target media, and the many elastic collisions which dominate neutron transport result in only small energy transfers (compared to neutron collisions with hydrogen atoms in water). Thus, the secondary neutrons are left with sufficient energy to continue producing charged target fragments well past 40 g/cm^2. Conversely, in water, there are far fewer neutrons produced, and the elastic collisions result in much larger energy transfers that render many of the neutrons incapable of producing further target fragments. It is important to note that the error curves in Fig. 7 do not grow without bound; they reach a maximum of about 75% near 725 g/cm^2 and then decline rapidly as the remaining neutrons have insufficient energy to produce any further target fragments. Error estimates for material

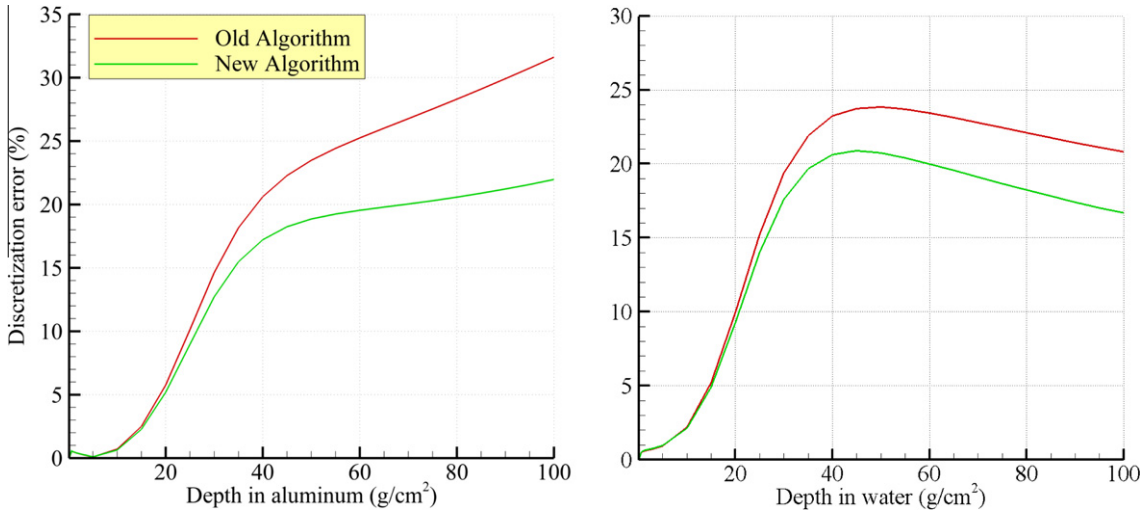

Fig. 7. Discretization error for dose equivalent as a function of depth for the light particle transport algorithms in aluminum (left pane) and water (right pane) exposed to the August 1972 King SPE.

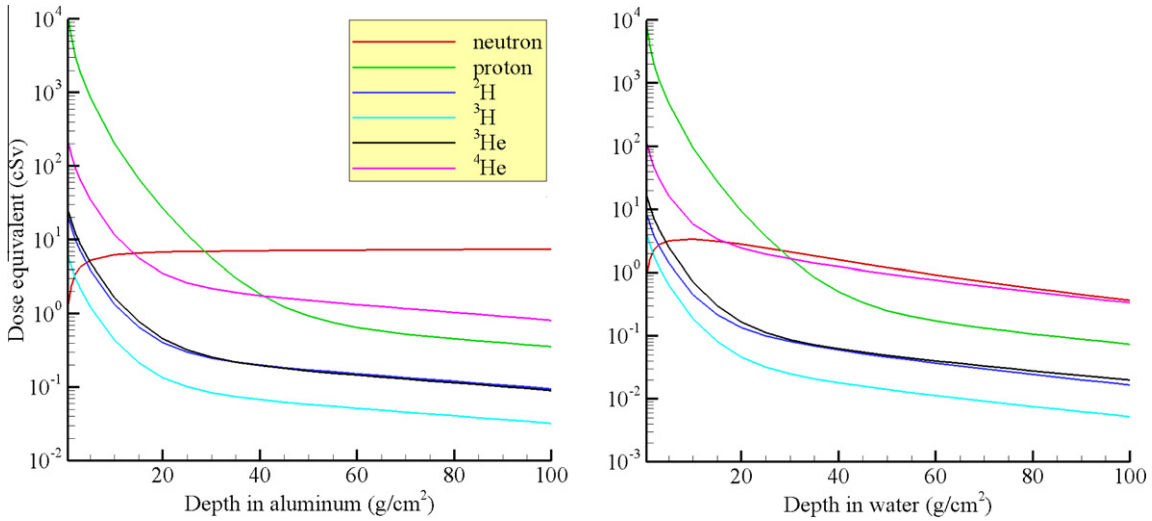

Fig. 8. Dose equivalent by particle type using the converged results at 100 g/cm^2 in aluminum (left pane) and water (right pane) exposed to the August 1972 King SPE.

thicknesses greater than 100 g/cm^2 are computationally expensive due to the long run-times associated with fine discretization parameters and large depths. This topic will be investigated in future work.

As stated previously, Fig. 6 shows that both methods, for a given energy grid, systematically under-predict dose equivalent values if step-sizes larger than 0.01 g/cm^2 are used. These step-sizes, including the coarse discretization parameter, $h = 0.5$ g/cm^2, commonly used in HZETRN, result in a systematic under-prediction of secondary target fragments; this under-prediction is the dominant source of discretization error in HZETRN.

Recall from Section 5 that two convergence criteria were identified for the light particle transport equation. The first criterion, in Eq. (16), (step-size much smaller than the nuclear mean free path) is trivially satisfied since nuclear mean free path lengths are typically on the order of many centimeters, but the second criterion, in Eq. (25), (step-size much smaller than the range), which has been identified in the present work, is not satisfied for low energy particles unless h is taken several orders of magnitude below 0.5 g/cm^2.

To show the error induced by choosing discretization parameters that violate the second criterion, a portion of the convergence test outlined previously is re-run with the minimum energy increased to 50 AMeV. This energy was chosen because 50 MeV protons have a range $\sim$2.9 g/cm^2, which should allow step-sizes of 0.5 g/cm^2 to be used with only minimal error.

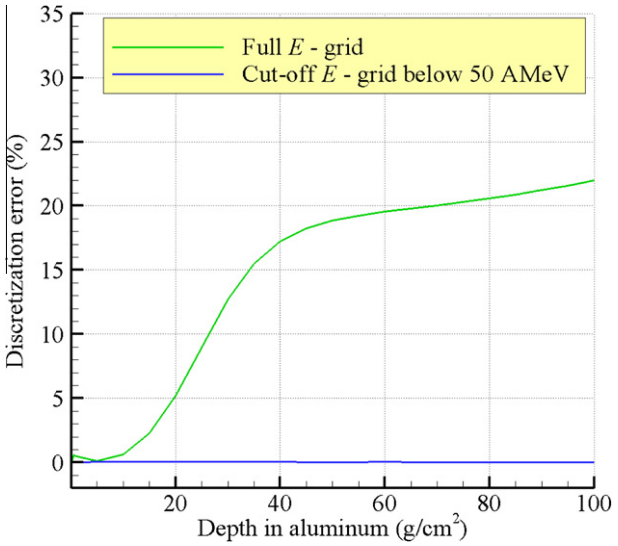

Fig. 9. Discretization error (%) caused by target fragments with energy less than 50 AMeV in aluminum exposed to the August 1972 King SPE.

Since the systematic under-prediction has been shown to be independent of the numerical algorithm, only the new light particle transport equation was used. Also, since the error was most prevalent in aluminum, the water target was not considered. For this comparison, the modified converged solution is defined as the results generated by the new method with a step-size of 2^{-11} g/cm^2 and the 753 point modified energy grid (E_{min} = 50 AMeV instead of 0.01 AMeV). The results generated by the new method using a step-size of 0.5 g/cm^2 and the modified 100 point energy grid will be compared to the modified converged results. The error comparisons are given in Fig. 9 along with the previous error curve shown in the left pane of Fig. 7. It is clear that neglecting the target fragments with energy less than 50 AMeV significantly reduces the discretization error in the light particle transport algorithm. The new error curve has a maximum of ~0.07% near 30 g/cm^2 of aluminum. Analytic solutions have been developed for low energy light and heavy target fragments [26,3]; however, these approaches include physical assumptions that may be less accurate for light particles at low energies. Future work will focus on resolving the low energy target fragment fluxes in HZETRN.

10. Convergence study for HZETRN in GCR environments

For GCR environments, the primary spectrum is composed of protons, ^{4}He, and heavier ions with energies extending up to 50 AGeV. In HZETRN, the heavy ion transport algorithm is used to transport the heavy ions along with their secondary fragments through the target media, and the light particle transport algorithm is used to transport the primary protons and ^{4}He along with the light projectile and target fragments. The light projectile fragments produced from the heavy ions are also included in the light particle transport algorithm, as discussed previously. A convergence analysis has never been performed, to the authors' knowledge, for the heavy ion or light particle transport algorithms in GCR environments. The convergence analysis described in the previous section is repeated for the heavy ion and light particle transport algorithms for GCR boundary conditions.

In this section, the total discretization error associated with the heavy ion transport algorithm and the old and new light particle transport algorithms in HZETRN is examined by conducting a coupled convergence analysis in step-size, h, and energy grid-size, N. For all comparisons, the round-off errors and interpolation routines mentioned in Section 5 have been fixed in the original algorithms. This will allow a direct comparison between the original and updated transport algorithms. The convergence analysis is identical to the one in Section 9 except that the 1977 solar minimum GCR environment is used, and the maximum energy is increased to E_{max} = 50 AGeV. The same step-sizes and energy grid-sizes are used. It is first shown that the heavy ion transport algorithm converges as a function of step-size and energy grid-size. The discretization error associated with the heavy ion transport algorithm for the discretization parameters (h = 0.5 g/cm^2 with 100 energy grid points) commonly used in HZETRN is also given. Next, the two light particle transport algorithms are compared. The new algorithm is shown to converge as a function of step-size and energy grid-size. It is also determined that the old algorithm converges as a function of step-size, but that larger energy grids are required to determine if the old algorithm converges as a function of energy grid-size. Finally, total discretization error estimates are given for discretization parameters commonly used in HZETRN. The errors are expressed as percent difference from a converged numerical solution.

In Fig. 10, dose equivalent as a function of depth in aluminum and water is given for the heavy ion transport algorithm coupled to both of the light particle transport algorithms and all of the discretization parameters. The plot legends have been removed because there are 132 different curves, many of which are overlapping. The spread in the data at 100 g/cm^2 in

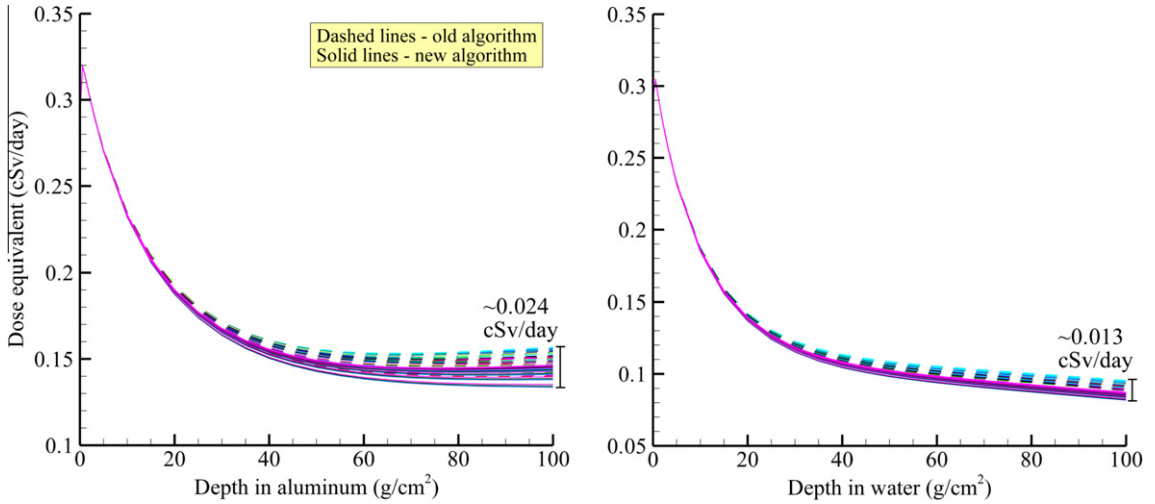

Fig. 10. Dose equivalent versus depth in aluminum (left pane) and water (right pane) exposed to the 1977 solar minimum GCR computed with both transport algorithms and all discretization parameters.

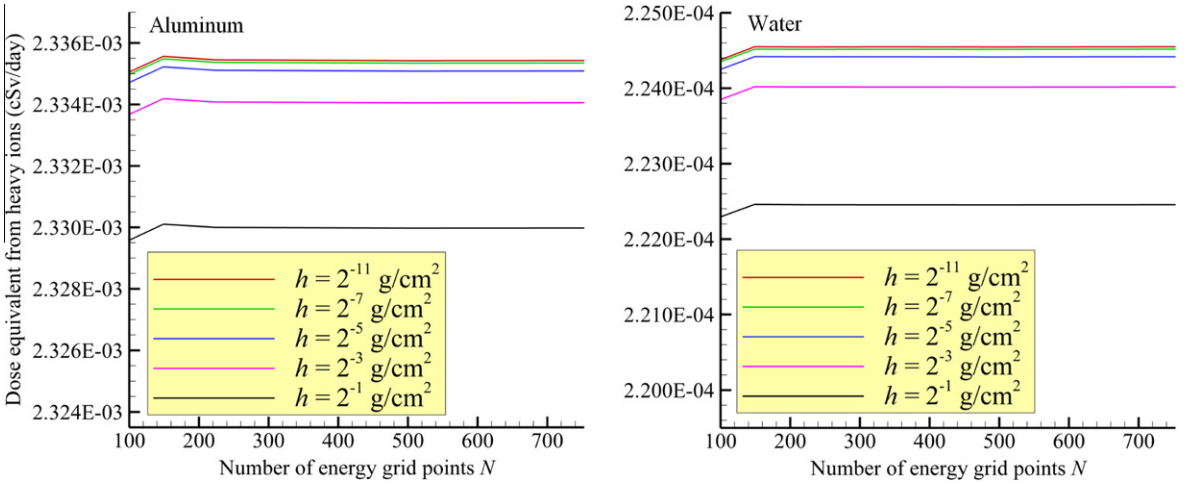

Fig. 11. Dose equivalent from heavy ions versus energy grid-size at 100 g/cm^2 in aluminum (left pane) and water (right pane) exposed to the 1977 solar minimum GCR environment. Five different step-sizes were used.

aluminum is ~0.024 cSv/day (~17%), and the spread in the data at 100 g/cm^2 in water is ~0.013 cSv/day (~15%). As before, both methods with the various discretization parameters produce similar results, and the errors appear to be slowly increasing as a function of depth in the material. Slightly larger errors are once again found in aluminum.

In Fig. 11, the contribution to dose equivalent from heavy ions at 100 g/cm^2 in aluminum and water is plotted as a function of the energy grid-size, N, for five step-sizes. The step-sizes were chosen to reduce data overlap and improve plot clarity. In Fig. 12, the contribution to dose equivalent from heavy ions at 100 g/cm^2 in aluminum and water is plotted as a function of the step-size, h, for all of the energy grids. Figs. 11 and 12 show that the heavy ion marching algorithm reaches an asymptotic solution for step-sizes less than 0.01 g/cm^2 and energy grids with greater than 250 points. It is concluded that the heavy ion transport algorithm converges as a function of step-size and energy grid-size.

In order to quantify the discretization error associated with the heavy ion transport algorithm, consider the contribution to dose equivalent from heavy ions only, and define the converged heavy ion solution as the results obtained using 753 energy grid points and a step-size of 2^{-11} g/cm^2. The step-size, h = 0.5 g/cm^2, and energy grid-size, N = 100, are once again chosen as the coarse discretization parameters.

The discretization error is expressed as the percent difference between the results generated with the coarse parameters and the converged solution. As before, this expression of discretization error is relevant for space radiation applications where physics modeling errors, numerical errors, and uncertainties are often expressed in terms of percents. To be clear,

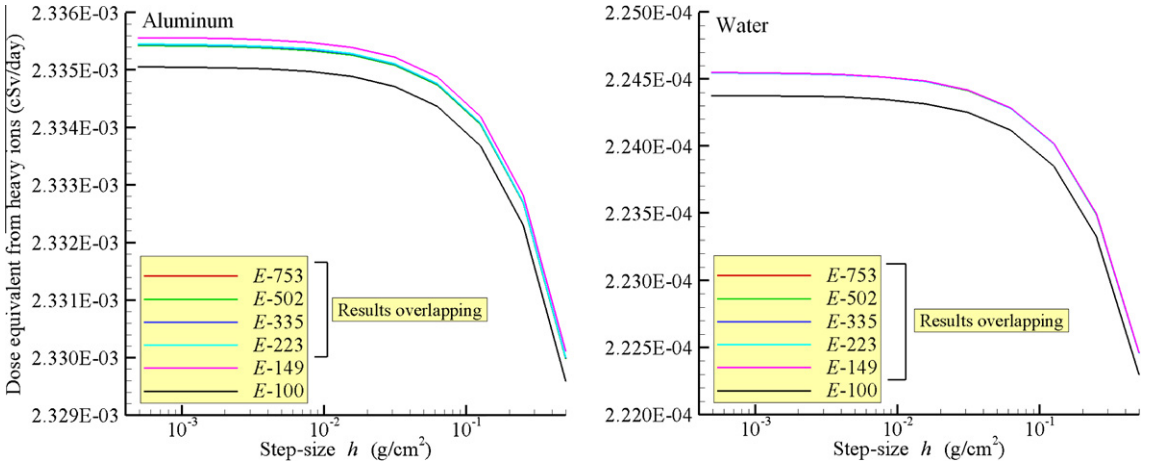

Fig. 12. Dose equivalent from heavy ions versus step-size at 100 g/cm^2 in aluminum (left pane) and water (right pane) exposed to the 1977 solar minimum GCR environment. All of the different energy grids were used.

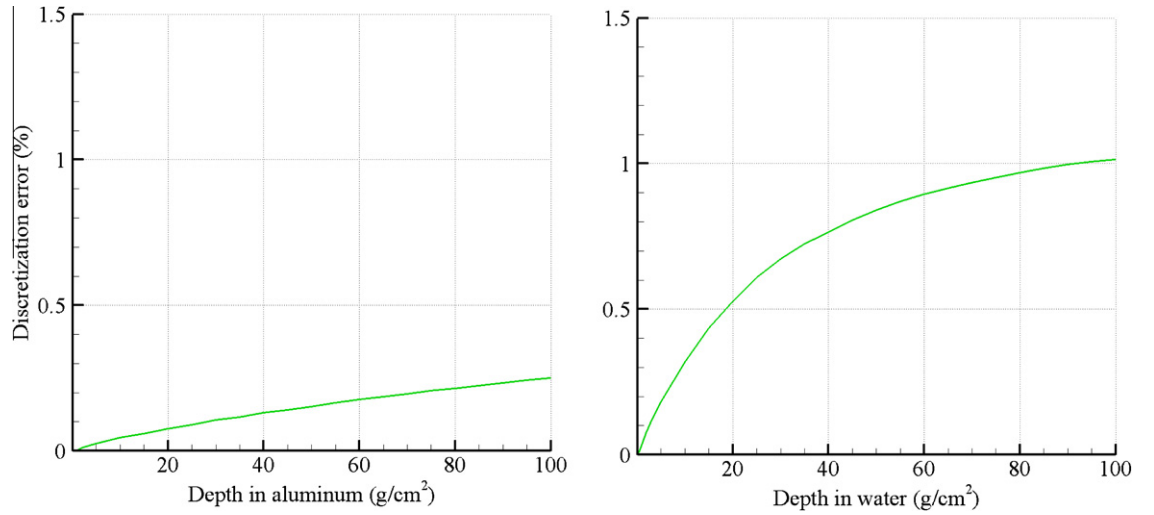

Fig. 13. Discretization error for dose equivalent as a function of depth for the heavy ion transport algorithm in aluminum (left pane) and water (right pane) exposed to the 1977 solar minimum GCR environment.

these discretization error estimates were obtained using only the heavy ion contribution to dose equivalent. The error caused by the light particle transport algorithm has not been included yet. The results are shown in Fig. 13 for the aluminum and water targets. The discretization errors are bounded over the depths shown by 0.3% in aluminum and 1.1% in water. Future work will focus on quantifying the discretization error depths greater than 100 g/cm^2.

In Fig. 14, total dose equivalent from heavy ions and light particles at 100 g/cm^2 in aluminum and water is plotted as a function of the energy grid-size, N, for three step-sizes. The step-sizes were chosen to reduce data overlap and improve plot clarity. In Fig. 15, dose equivalent at 100 g/cm^2 in aluminum and water is plotted as a function of the step-size, h, for all of the energy grids. Figs. 14 and 15 show that the new light particle transport algorithm coupled to the heavy ion transport algorithm reaches an asymptotic solution for step-sizes less than 0.01 g/cm^2 and energy grids with greater than 300 points. It is concluded that the new light particle transport algorithm converges as a function of step-size and energy grid-size. Conversely, while the old algorithm appears to converge as a function of step-size, it has not converged as a function of energy grid-size if 753 grid points are used. This does not mean that the old algorithm will not converge. All that can be said is that an asymptotic solution is not achieved by the old algorithm if as many as 753 energy grid points are used. This would indicate that the new method is more accurate and converges faster as a function of energy grid-size.

In order to quantify the discretization error associated with the algorithms, define the converged solution as the results obtained with the new light particle transport algorithm (coupled to the heavy ion algorithm) using 753 energy grid points and a step-size of 2^{-11} g/cm^2. The step-size, $h = 0.5$ g/cm^2, and energy grid-size, $N = 100$, are once again chosen as the coarse discretization parameters. The discretization error is expressed as the percent difference between the results generated with

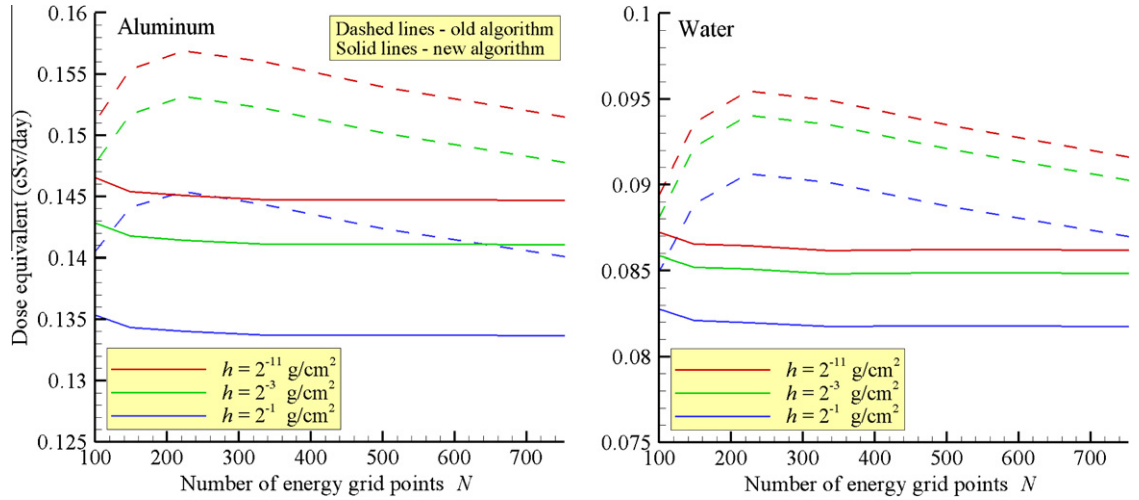

Fig. 14. Dose equivalent versus energy grid-size at 100 g/cm^2 in aluminum (left pane) and water (right pane) exposed to the 1977 solar minimum GCR environment. Both transport algorithms were used with three different step-sizes.

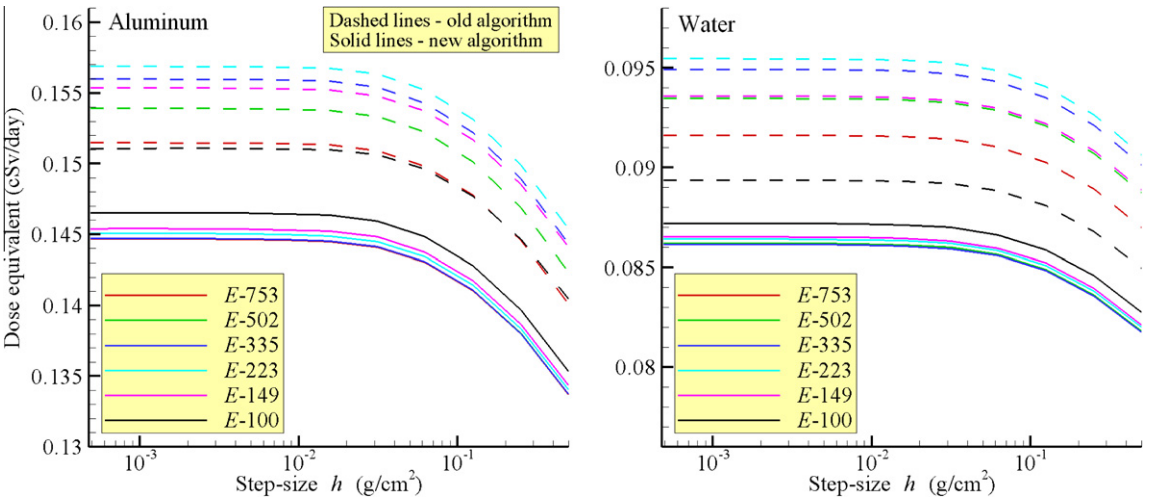

Fig. 15. Dose equivalent versus step-size at 100 g/cm^2 in aluminum (left pane) and water (right pane) exposed to the 1977 solar minimum GCR environment. Both transport algorithms were used with six different energy grids.

the coarse parameters and the converged solution. These error estimates were obtained using total exposure quantities (heavy ions and light particles included), thus the discretization error from the heavy ion transport algorithm, though small, is included. The results are shown in Fig. 16 for the aluminum and water targets. The discretization errors are bounded over the depths shown by 6.5% in aluminum and 3.9% in water.

The errors shown for the old method are misleadingly small. First, recall that the old method has not reached an asymptotic solution if 753 energy grid points are used; thus, it converges more slowly than the new algorithm as a function of energy grid-size. Second, the errors reported here are dependent on the choice of the converged solution. In this case, the energy discretization error and the spatial discretization error in the old algorithm are competing errors and therefore produce misleading error estimates when compared to the given converged solution. As before, the errors are slowly increasing as a function of depth in the material, and it is expected that these errors will reach a maximum after the majority of the primary ions and secondary projectile fragments have come to rest. Future work will focus on quantifying the discretization error depths greater than 100 g/cm^2.

11. Run time comparisons

In this section, the run-times of the old and new transport algorithms are compared for three applications in which HZETRN is commonly used. All simulations were run on a desktop computer with 4 quad-core AMD Opteron Processor

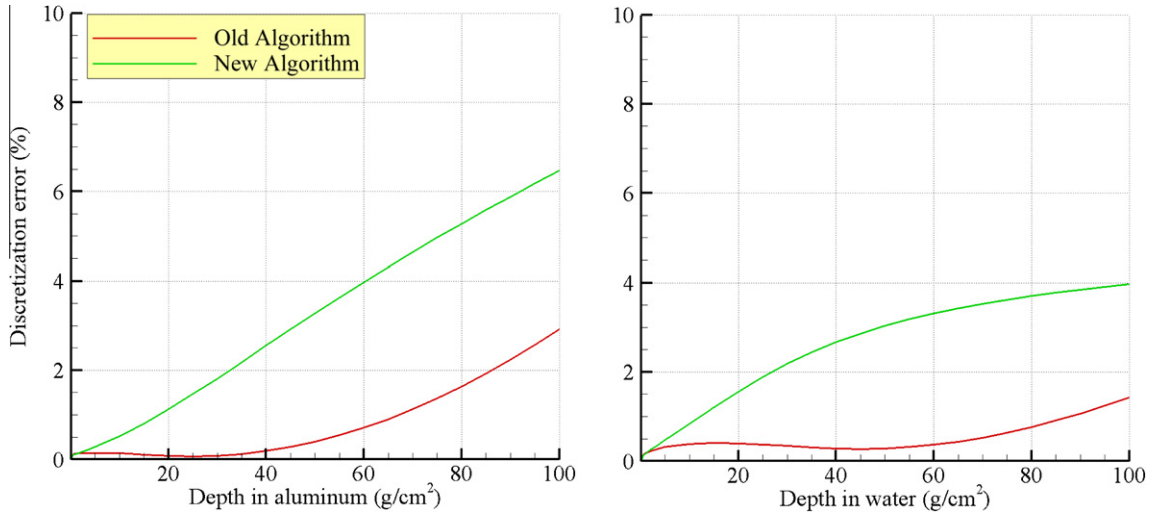

Fig. 16. Discretization error (%) for dose equivalent as a function of depth for both algorithms in aluminum and water exposed to the 1977 solar minimum GCR environment.

Table 1
Run time comparisons for old and new algorithms in one, two, and three layer slabs exposed to SPE and GCR environments. The reduction factor is the ratio of the old method run-time to the new method run-time.

	1 layer (s)		2 layers (s)		3 layers (min)	
	SPE	GCR	SPE	GCR	SPE	GCR
Old method	62.0	77.0	1272	926	440	173
New method	0.7	9.0	15	108	5	21
Reduction factor	88.5	8.5	85	9	88	8

8356 chips and 131 GB of memory. The discretization parameters used in each case were $h = 0.5$ g/cm^2 and 100 energy grid points.

In the first application, HZETRN is used to compute fluence, dose, or dose equivalent as a function of depth in a single layer of some material. This type of calculation might be done to analyze the radiation protection properties of a slab of some material or to generate a simplified interpolation database. In this case, consider separately aluminum exposed to the August 1972 King SPE and the 1977 solar minimum GCR spectrum. For the SPE environment, results are stored at 21 depths from 0.0 g/cm^2 to 100.0 g/cm^2. For the GCR environment, results are stored at 11 depths from 0.0 g/cm^2 to 100.0 g/cm^2. The difference in the number of depths is related to the rapid decline of the SPE dosimetric quantities over the first few g/cm^2 of shielding [1]. The next application is a two-layer simulation in which results are stored on a two dimensional grid of points covering every combination of first layer thicknesses followed by second layer thicknesses. In this case, consider a first layer of aluminum followed by a second layer of water. This simulation is typically used to model a shielding structure (aluminum) surrounding a human phantom (water). The spatial grids mentioned above for the SPE and GCR environments are used in this application. The final application is a three-layer simulation in which results are stored on a three dimensional grid of points covering every combination of first, second, and third layer thicknesses. In this case, consider a first layer of aluminum, a second layer of polyethylene, and a third layer of water. This simulation is typically used to model a shielding structure (aluminum) with a secondary shield (polyethylene) surrounding a human phantom (water). The spatial grids mentioned above for the SPE and GCR environments are used in this application. The run-times for all three cases are given in Table 1.

The run-times in Table 1 show that the new method is much faster than the old method in both SPE and GCR environments. The new method is nearly 90 times faster for SPE simulations and nearly 10 times faster for GCR simulations. It should be noted that run-times in the old method are dependent on the atomic complexity of the target material. For targets with many atomic species, the cross sections computed within the transport procedure will require more time and therefore slow the transport procedure. However, in the new method, cross sections are pre-computed, and therefore, increased atomic complexity does not affect the run-times. Since the materials considered here had at most two atomic species (water, polyethylene), the reduction factors given here are conservative.

12. Conclusions and future work

In this paper, a detailed derivation of the numerical marching algorithms used for light particles and heavy ions in HZETRN was given. Components of the derivation that were previously absent in the documentation were discussed in

detail. A new numerical method was presented for the light particle transport algorithm. In general, the new method requires fewer interpolations per step.

The impact of single precision round-off error and interpolation on code stability and accuracy was discussed. Round-off error was shown to be problematic for some of the light particle production cross sections. A new interpolation routine used in both the heavy ion and light particle transport algorithm was presented, and the improved efficiency and robustness of the routine was demonstrated.

A convergence study was conducted to determine if the old and new algorithms converge as a function of step-size and energy grid-size and to quantify the discretization error associated with both algorithms. The old and new algorithms were shown to converge to the same results for the SPE environment, and the improved accuracy of the new method was demonstrated. Total discretization error on dose equivalent at 100 g/cm^2 was reduced from 31% to 21% in aluminum and from 20% to 15% in water for commonly used energy grids. For the GCR environment, the heavy ion transport algorithm was first shown to converge as a function of step-size and energy grid-size, and discretization error estimates were bounded over the depths shown by approximately 1% at 100 g/cm^2 in aluminum and water. The new light particle transport algorithm was also shown to converge as a function of step-size and energy grid-size. The old algorithm was shown to converge as a function of step-size, and it was concluded that energy grids with more than 753 points are required to show convergence in the energy domain. This indicates that the new method converges faster and is more accurate in GCR environments. Total discretization error on dose equivalent at 100 g/cm^2 was 6% in aluminum and 4% in water for the new method.

The importance of low energy target fragments on discretization error was shown by neglecting all particles with energy less than 50 AMeV in the transport procedure. The error estimates for the cut-off energy grid were negligible compared to the full energy grid. This indicates that the dominant source of discretization error in HZETRN is caused by low energy target fragmentation. Further, to the author's knowledge, only the convergence criterion in Eq. (16) (step-size smaller than the nuclear mean free path length) has been addressed in the literature. The second convergence criterion in Eq. (25) (step-size smaller than the fragment range), found here in the derivation of the numerical procedures, has never been explicitly written until now. This work definitively shows the presence of two convergence criteria, and that previous convergence studies never addressed the second criterion.

Run time comparisons between the old and new algorithms showed large improvements for three applications in which HZETRN is commonly used. The new algorithm was found to be approximately 90 times faster for SPE simulations and approximately 10 times faster for GCR simulations.

Future work should focus on further reducing discretization error in HZETRN by developing more robust methods for handling the transport of low energy target fragments. While physics modeling errors associated with the straight ahead approximation may exceed the current numerical error at depths past 100 g/cm^2, there is still a need to reduce the numerical error as long as the current model is used in studies with such large material depths [12,28].

Acknowledgments

This research was sponsored by NASA Research Grant NNL06AA14A and NNX09AR20A. The authors thank William Oberkampf for his guidance and helpful discussion.

References

[1] B. Anderson, S.R. Blattnig, M.S. Clowdsley, Numerical uncertainty quantification for radiation analysis tools, in: Society of Automotive Engineers International Conference on Environmental Systems, 07ICES-92, 2007.
[2] Von H. Bethe, Zur Theorie des Durchgangs schneller Korpuskularstraheln durch Materie, Annals of Physics 5 (1930) 325–400.
[3] F.A. Cucinotta, Calculations of cosmic-ray helium transport in shielding materials, NASA Technical Paper 3354, 1993.
[4] F.A. Cucinotta, J.W. Wilson, P. Saganti, X. Hu, M.Y. Kim, T. Cleghorn, C. Zeitlin, R.K. Tripathi, Isotopic dependence of GCR fluence behind shielding, Radiation Measurements 41 (2006) 1235–1249.
[5] R. Haberman, Elementary Applied Partial Differential Equations, Prentice Hall, New Jersey, 1998.
[6] J.H. Heinbockel, T.C. Slaba, S.R. Blattnig, R.K. Tripathi, L.W. Townsend, T. Handler, T.A. Gabriel, L.S. Pinsky, B. Reddell, M.S. Clowdsley, R.C. Singleterry, J.W. Norbury, F.F. Badavi, S.K. Aghara, Comparison of the radiation transport codes HZETRN, HETC-HEDS and FLUKA using the February 1956 Webber SPE spectrum, NASA Technical Paper 2009-215560, 2009.
[7] J.H. Heinbockel, T.C. Slaba, R.K. Tripathi, S.R. Blattnig, J.W. Norbury, F.F. Badavi, L.W. Townsend, T. Handler, T.A. Gabriel, L.S. Pinsky, B. Reddell, A.R. Aumann, Comparison of the transport codes HZETRN, HETC and FLUKA using the 1977 GCR solar minimum spectra, NASA Technical Paper 2009-215941, 2009.
[8] J.H. King, Solar proton fluences for 1977–1983 space missions, Journal of Spacecraft and Rockets 11 (1974) 401–408.
[9] S.L. Lamkin, G.S. Khandelwal, J.L. Shinn, J.W. Wilson, Numerical methods for high energy nucleon transport, in: Proceedings of the Topical Meeting on New Horizons in Radiation Protection and Shielding, Report Number OCLC 26290867, 1992.
[10] S.L. Lamkin, G.S. Khandelwal, J.L. Shinn, J.W. Wilson, Space proton transport in one dimension, Nuclear Science and Engineering 116 (1994) 291–299.
[11] G.I. Marchuk, V.I. Lebedev, Numerical Methods in the Theory of Neutron Transport, Harwood Academic Publishers, New York, 1986.
[12] C.J. Mertens, B.T. Kress, M. Wiltberger, S.R. Blattnig, T.C. Slaba, S.C. Solomon, M. Engel, Geomagnetic influence on aircraft radiation exposure during a solar energetic particle event in October 2003, Space Weather 8 (2010) S03006, doi:10.1029/2009SW000487.
[13] NASA, NASA Standards for Modeling and Simulation, NASA Standard 7009, 2008.
[14] P.M. O'Neill, Badhwar–O'Neill, galactic cosmic ray model update based on advanced composition explorer (ACE) energy spectra from 1997 to present, Advances in Space Research 37 (2006) 1727–1733.
[15] C.J. Roy, Review of code and solution verification procedures for computational simulation, Journal of Computational Physics 205 (2005) 131–156.
[16] J.L. Shinn, J.W. Wilson, M. Weyland, F.A. Cucinotta, Improvements in the computational accuracy of BRYNTRN (a Baryon transport code), NASA Technical Paper 3093, 1991.

[17] J.L. Shinn, S. John, R.K. Tripathi, J.W. Wilson, L.W. Townsend, J.W. Norbury, A fully energy-dependent HZETRN (a galactic cosmic-ray transport code), NASA Technical Paper 3243, 1992.
[18] T.C. Slaba, S.R. Blattnig, F.F. Badavi, Faster and more accurate transport procedures for HZETRN, NASA TP 2010-216213, 2010.
[19] T.C. Slaba, G.D. Qualls, M.S. Clowdsley, S.R. Blattnig, L.C. Simonsen, S.A. Walker, R.C. Singleterry, Analysis of mass averaged tissue doses in CAM, CAF, MAX, and FAX, Advances in Space Research 45 (2010) 866–883.
[20] T.C. Slaba, S.R. Blattnig, M.S. Clowdsley, S.A. Walker, F.F. Badavi, An improved neutron transport algorithm for HZETRN, Advances in Space Research 46 (2010) 800–810.
[21] J.W. Wilson, S.L. Lamkin, Perturbation theory for charged-particle transport in one dimension, Nuclear Science and Engineering 57 (1975) 292–299.
[22] J.W. Wilson, Analysis of the theory of heavy ion transport, NASA Technical Note D-8381, 1977.
[23] J.W. Wilson, F.F. Badavi, Methods of galactic heavy ion transport, Radiation Research 108 (1986) 231–237.
[24] J.W. Wilson, L.W. Townsend, A benchmark for galactic cosmic-ray transport codes, Radiation Research 114 (1988) 201–206.
[25] J.W. Wilson, L.W. Townsend, J.E. Nealy, S.Y. Chun, B.S. Hong, W.W. Buck, S.L. Lamkin, B.D. Ganapol, F. Khan, F.A. Cucinotta, BRYNTRN: a Baryon transport model, NASA Technical Paper 2887, 1989.
[26] J.W. Wilson, L.W. Townsend, W. Schimmerling, G.S. Khandelwal, F. Khan, J.E. Nealy, F.A. Cucinotta, L.C. Simonsen, J.L. Shinn, J.W. Norbury, Transport Methods and Interactions for Space Radiations, NASA Reference Publication 1257, 1991.
[27] J.W. Wilson, F.F. Badavi, F.A. Cucinotta, J.L. Shinn, G.D. Badhwar, R. Silberberg, C.H. Tsao, L.W. Townsend, R.K. Tripathi, HZETRN: description of a free-space ion and nucleon transport and shielding computer program, NASA Technical Paper 3495, 1995.
[28] J.W. Wilson, P. Goldhagen, V. Rafnsson, J.M. Clem, G.D. Angelis, W. Friedberg, Overview of atmospheric ionizing radiation (AIR) research: SST-present, Advances in Space Research 32 (2003) 3–16.
[29] J.W. Wilson, R.K. Tripathi, C.J. Mertens, S.R. Blattnig, M.S. Clowdsley, F.A. Cucinotta, J. Tweed, J.H. Heinbockel, S.A. Walker, J.E. Nealy, Verification and validation: high charge and energy (HZE) transport codes and future development, NASA Technical Paper 2005-213784, 2005.
[30] J.W. Wilson, R.K. Tripathi, F.F. Badavi, F.A. Cucinotta, Standardized radiation shield design method: 2005 HZETRN, SAE ICES 2006-18, 2006.